submitted to *Geophys. J. Int.*

Can we use seismic reflection data to infer the interconnectivity of fracture networks?

J. Germán Rubino[1⋆], Nicolás D. Barbosa[2], Jürg Hunziker[2], and Klaus Holliger[2]

[1] *CONICET, Centro Atómico Bariloche - CNEA, San Carlos de Bariloche, Argentina,*

[2] *Institute of Earth Sciences, University of Lausanne, Lausanne, Switzerland*

SUMMARY

While variations of seismic reflection amplitudes with incidence angle (AVA) and azimuth have been widely used to provide information on geometric characteristics of fractures, this attribute has, as of yet, not been linked to fracture interconnectivity, which tends to govern the hydraulic property of the affected formation. This is due to limitations of the forward models considered to represent the corresponding seismic responses. Based on a poroelastic upscaling procedure and a subsequent plane-wave analysis, we show for the first time that seismic reflection coefficients are highly sensitive to fracture interconnectivity. Moreover, our results suggest that crossplots of commonly employed AVA coefficients can be used to delineate regions of fractured formations with higher or lower fracture interconnectivity. This sensitivity is due to changes of the stiffening effect of the fluid contained within interconnected fractures in response to wave-induced fluid pressure diffusion (FPD), a physical process that has not been previously accounted for in seismic reflection analyses.

Key words: Fracture and flow – Seismic anisotropy – Numerical modelling – Acoustic properties

⋆ Corresponding author

1 INTRODUCTION

Fractures are ubiquitous in the shallower parts of the Earth's crust and they usually provide preferential pathways for the flow of pore fluids. For this reason, the detection of fractures in general and the assessment of their interconnectivity in particular are tasks of great importance with applications in groundwater and contaminant hydrology, nuclear waste storage, CO_2 sequestration, and hydrocarbon exploration and production, amongst others (e.g., Liu et al. 2000; Nelson 2001; Maultzsch et al. 2003).

The seismic method constitutes a key tool to detect and characterize fractures in a non-invasive manner and on a relatively large scale. In particular, variations of seismic reflection amplitudes with incidence angle (AVA) and azimuth are often used to provide geometric information on fractures (e.g., Liu & Martinez 2012). In this context, there are some studies in the literature linking seismic and hydraulic properties of fractured formations (e.g., Boadu 2000; Jakobsen et al. 2007; Ali & Jakobsen 2014). These works do, however, only consider the role played by the length, aperture, and orientation of the fractures and neglect the influence of interconnectivity, which is a critical parameter controlling the hydraulic properties of the formation (Berkowitz et al. 2000). In fact, regardless of the geometric characteristics of the individual fractures, if their interconnectivity is low, the effective hydraulic properties of the formation will be controlled by the permeability of the embedding background material.

Despite its importance, as far as we know, there are no theoretical analyses or experiments explicitly linking AVA data to fracture interconnectivity, which is due to inherent limitations of the models employed to represent the seismic response of these media. Indeed, in the context of the theory of elasticity, fracture intersections are predicted to have negligible influence on the effective elastic properties and, therefore, on seismic data of fractured formations (Grechka & Kachanov 2006). Other popular models consider the impact of fluid-pressure diffusion (FPD) between the fractures and the embedding porous background rock, but do not account for fracture interconnectivity effects (e.g., Chapman 2009; Bakulin et al. 2000). However, when a seismic wave travels through a fluid-saturated porous formation containing a fracture network, FPD within connected fractures can arise, affecting significantly the characteristics of the propagating seismic wave (Rubino et al. 2013, 2017). Indeed, Rubino et al. (2017) demonstrated that the presence of connected fractures tends to modify the velocity anisotropy of the probed formation in the seismic frequency band. These authors showed that, for such frequencies, these fracture interconnectivity effects are not manifested as seismic attenuation or dispersion, but in the form of variations of the compliance of connected fractures due to changes of the stiffening effect of the fluid present in the fractures in response to FPD. That is, when a seismic wave compresses a disconnected fluid-saturated fracture, it increases its fluid pressure. However, if the fracture is connected to another one of different orientation, the fluid pressure increase will be lower, which implies an increase of fracture compliance and a corresponding impact on the seismic velocity.

The results of Rubino et al. (2017) therefore indicate that seismic data encode valuable information on the interconnectivity of fracture networks, which is currently ignored and, potentially, misinterpreted. In spite of this, the corresponding effects on seismic reflection data remain unexplored.

In this paper, we seek to shed some light on the sensitivity of seismic reflection data to the interconnectivity of fracture networks. To this end, we first use a numerical upscaling procedure based on the theory of poroelasticity (Biot 1941) to determine the effective stiffness matrices of 2D models of fractured formations and accounting for fracture interconnectivity effects. Next, we perform a plane-wave analysis to determine the amplitudes of seismic waves reflected from the top of the considered fractured formations, which are characterized by their effective stiffness matrices. We analyze the results for formations containing sets of conjugate fractures characterized by different orientations and varying degrees of interconnectivity.

2 METHODOLOGY

We consider a plane P-wave incident on a fractured formation and compute the reflection coefficients at its top boundary (Figure 1). The fractures are of mesoscopic scale, that is, they are much larger than the grain and pore sizes, but much smaller than the prevailing seismic wavelengths. This implies that the resolution of seismic data is insufficient for directly imaging the fractures, which, instead, manifest themselves through an increase of the overall attenuation, dispersion, and anisotropy (e.g., Liu & Martinez 2012). To obtain the AVA response, we first employ a numerical upscaling procedure (Rubino et al. 2016; Hunziker et al. 2018) to determine an effective anisotropic viscoelastic solid representing the fractured formation. Next, we solve the anisotropic viscoelastic equations of motion in the space-frequency domain for a plane P-wave incident at a given angle θ.

Due to the high computational cost of 3D numerical simulations, we consider a 2D scenario under plane strain conditions normal to the x-y plane (Figure 1). This implies that the fractures have the same strike and are sufficiently long in the z direction so that the strains along this axis are negligible compared with those along the other two axes. From a practical point of view, the computed reflection coefficients are representative for a seismic survey perpendicular to the strike of the fractures.

2.1 Effective properties of the fractured formation

We assume that there are no significant variations of the statistical properties of the geometric characteristics of the fractures throughout the formation. This implies that the fractured formation behaves as a homogeneous medium with effective properties at the wavelength scale. The presence of hydraulically-open fractures causes (i) a reduction of seismic velocities due to their large compli-

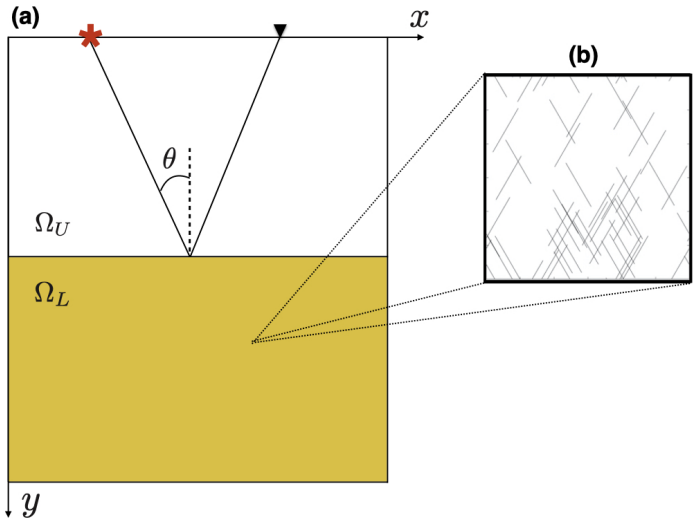

Figure 1. (a) Schematic illustration of a homogeneous medium Ω_U overlying a fractured formation Ω_L whose effective properties are obtained through a numerical upscaling procedure. (b) Blow-up depicting a representative elementary volume (REV) with partially interconnected mesoscopic fractures.

ances, (ii) anisotropy due to their elongated shapes and preferential orientations, and (iii) attenuation and dispersion in response to FPD produced by their strong mechanical contrast with respect to the embedding background (Rubino et al. 2013, 2014, 2017). These FPD processes occur not only between the fractures and the embedding porous background, but also within connected fractures, which makes the seismic response of the media sensitive to fracture interconnectivity. All these effects can be captured in the framework of viscoelasticity by using a frequency-dependent effective stiffness matrix $C_{ij}^{\text{eff}}(\omega)$ (Rubino et al. 2016). In 2D and for the coordinate system defined in Figure 1, the effective stress-strain relations can be described by

$$\begin{pmatrix} \sigma_{11} \\ \sigma_{22} \\ \sigma_{12} \end{pmatrix} = \begin{pmatrix} C_{11}^{\text{eff}} & C_{12}^{\text{eff}} & C_{16}^{\text{eff}} \\ C_{12}^{\text{eff}} & C_{22}^{\text{eff}} & C_{26}^{\text{eff}} \\ C_{16}^{\text{eff}} & C_{26}^{\text{eff}} & C_{66}^{\text{eff}} \end{pmatrix} \begin{pmatrix} \epsilon_{11} \\ \epsilon_{22} \\ 2\epsilon_{12} \end{pmatrix}, \tag{1}$$

with σ_{ij} and ϵ_{ij} being the elements of the stress and strain tensors at the wavelength scale. The propagation of seismic waves though the fractured formation can be described by eq. 1, together with the anisotropic viscoelastic equation of motion.

To determine the effective stiffness matrix C_{ij}^{eff}, we employ the implementation of Hunziker et al. (2018) of the numerical upscaling procedure presented by Rubino et al. (2016). That is, we consider a square sample representative of the formation of interest containing fractures in the mesoscopic scale range, as schematically shown in Figure 1b. The fractures are modelled as highly compliant porous media characterized by very high porosity and permeability and they are in hydraulic communication

with the embedding porous background (Rubino et al. 2013). The sample is then subjected to three relaxation tests that provide the required information on the effective viscoelastic representation of the probed medium (Rubino et al. 2016; Hunziker et al. 2018). First, homogeneous time-harmonic normal displacements of opposite direction are applied on the top and bottom boundaries. The second test is similar to the previous one, but the normal displacements are applied to the lateral boundaries. Finally, the third test consists of oscillatory shear displacements along the upper and lower boundaries in opposite directions. Unless mentioned otherwise, for all these tests we consider periodic boundary conditions for the solid displacement and the fluid pressure, and antiperiodic boundary conditions for the traction and fluid flux.

The behavior of the probed fractured rock to the relaxation tests is obtained in the context of Biot's theory of quasistatic poroelasticity (Biot 1941), which naturally accounts for FPD effects. Locally, the total stress equilibrium and Darcy's law are then to be fulfilled simultaneously, which in the space-frequency domain yields

$$\nabla \cdot \boldsymbol{\sigma}^{\mathbf{pm}} = \mathbf{0}, \tag{2}$$

$$\nabla p_f = -i\omega \frac{\eta}{\kappa} \boldsymbol{w}, \tag{3}$$

where $\boldsymbol{\sigma}^{\mathbf{pm}} \equiv \left(\sigma_{ij}^{\mathrm{pm}}\right)$ represents the total stress tensor of the porous medium, $\boldsymbol{w}$ the average relative fluid displacement per unit volume of bulk material, p_f the fluid pressure, κ the permeability, η the viscosity of the pore fluid, and ω is the angular frequency. The stress-strain relations are given by (Biot 1962)

$$\sigma_{ij}^{\mathrm{pm}} = 2\mu\epsilon_{ij}^{\mathrm{pm}} + \delta_{ij}\left(\lambda_c \nabla \cdot \boldsymbol{u}^{\mathbf{pm}} - \alpha M \zeta\right), \tag{4}$$

$$p_f = -\alpha M \, \nabla \cdot \boldsymbol{u}^{\mathbf{pm}} + M\zeta, \tag{5}$$

where $\boldsymbol{u}^{\mathbf{pm}}$ is the average solid displacement of the porous material, $\epsilon_{ij}^{\mathrm{pm}} = \frac{1}{2}\left(\partial u_i^{\mathrm{pm}}/\partial x_j + \partial u_j^{\mathrm{pm}}/\partial x_i\right)$ the strain tensor, and $\zeta = -\nabla \cdot \boldsymbol{w}$ is a measure of the local change in the fluid content. In equation (4), μ is the shear modulus of the saturated material, which is equal to that of the dry frame μ_m. The Biot effective stress coefficient α, the Biot modulus M, and the undrained Lamé parameter λ_c can be computed as functions of the properties of the solid grains, dry matrix and pore fluid of the considered material (e.g., Mavko et al. 1998).

The solid and relative fluid displacements in response to the three tests are numerically approximated by solving equations 2 to 5 under corresponding boundary conditions. Under the assumption that the fractured sample can be represented by an effective homogeneous anisotropic viscoelastic solid, the volume averages of the stress and strain components resulting from each test are linked through an effective stiffness matrix, as shown in equation 1. Please notice that, in this equation, we should consider $\sigma_{ij} \equiv < \sigma_{ij}^{\mathrm{pm}} >$ and $\epsilon_{ij} \equiv < \epsilon_{ij}^{\mathrm{pm}} >$, where $<>$ denotes the volume average of the

considered quantity. The effective stiffness matrix C_{ij}^{eff} is then computed, for each frequency, following a least-squares procedure (Rubino et al. 2016). This upscaling procedure has been implemented as a finite element code called "Parrot", which is able to handle complex fracture geometries (Hunziker et al. 2018; Favino et al. 2020).

2.2 Reflection coefficients at the top of the fractured formation

Once the effective viscoelastic properties of the fractured formation have been determined, we can explore the characteristics of reflected seismic waves in the context of the theory of viscoelasticity. With this aim, and assuming that the fractured formation and the overburden are much thicker than the predominant seismic wavelengths, we consider a plane interface separating two halfspaces Ω_U and Ω_L (Figure 1) to compute the reflection coefficients. For simplicity, we assume that the overburden Ω_U is elastic and isotropic, while the fractured medium Ω_L can be viscoelastic and characterized by any degree of anisotropy. Please notice that this medium is represented by the effective stiffness matrix C_{ij}^{eff}, which accounts for FPD effects.

We consider that a plane, harmonic, homogeneous P-wave arrives at the interface from Ω_U with an incidence angle θ measured with respect to the normal (see Figure 1). This perturbation generates four waves at the interface: reflected compressional and shear waves in Ω_U, and transmitted quasi-compressional and quasi-shear waves in Ω_L. The displacements in the upper halfspace are then caused by the contribution of the incident and reflected waves, while in the lower halfspace they are produced by the transmitted wavefield components. Such displacement vectors can be used to obtain the components of the strain tensor in each halfspace and, through the use of the corresponding stiffness matrix, the stress tensor for each media can be computed. By requiring the continuity of the particle displacements and normal and tangential stresses at the interface, a linear system of equations is obtained, which allows to obtain the amplitudes of the reflected and transmitted perturbations and, thus, the reflection coefficients. The details of this procedure are outlined in Appendix A.

3 NUMERICAL ANALYSIS

In this Section, we apply the previously described methodology to obtain the AVA responses of formations containing conjugate fractures. We consider different inclinations for the fractures and, in particular, contrasting degrees of connectivity to highlight the role played by this important characteristic of fracture networks.

3.1 Physical and geometric properties of the fracture networks

To explore the sensitivity of AVA to fracture interconnectivity, we consider two end-member-type models of fractured formations, which in the following are referred to as "low connectivity" and "high connectivity". These models have the same fracture density of 0.01, defined as the area covered by the fractures divided by the total area of the sample, and differ only in terms of the degree of interconnectivity. In the low connectivity case, we consider that, in the probed formation there are, on average, less than 0.28 fracture intersections per square meter measured in the considered x-y plane whereas, in the high connectivity case, more than 1.67 intersections. In both cases, the networks are composed of equal, randomly distributed, rectangular fractures with a length of 1.5 m and an aperture of 5 mm. Half of the fractures are oriented at an angle $-\alpha/2$ with respect to the vertical, whereas the remaining half at $+\alpha/2$, thus, forming intersection angles of α. Fracture sets of this type are representative of conjugate shear fractures, which tend to be oriented at the same angle with respect to the principal stress directions (e.g., Nelson 2001; Galvin et al. 2007). We focus the analysis on this kind of fracture sets because they are very common in the crust and are considered to control the fluid flow characteristics of the affected formation (e.g., Liu & Martinez 2012; Barton 2006). Overlying the fractured formation, we consider a homogeneous medium having the properties of the intact background that surrounds the fractures. The AVA response is then obtained at the interface separating the two media.

As fracture networks are very complex, corresponding REVs tend to be very large and their direct characterization can be computationally unfeasible. To deal with this issue, we consider samples having sizes smaller than those of corresponding REVs and compute the reflection coefficients in a Monte Carlo fashion, which provides the representative properties through averaging (Rubino et al. 2009). For the two end-member-type models, we then consider an ensemble of square samples of 6 m sidelength, which contain 50 fractures and only differ in terms of their fracture interconnectivity: the low-connectivity samples contain less than 10 intersecting fractures, whereas the high-connectivity ones contain more than 60 intersections. Like this, the two sets of fractures satisfy the previously given definition of low and high connectivity models in terms of the average number of fracture intersections per square meter. In addition, the considered distributions of fractures are periodic with respect to the boundaries, in accordance with the boundary conditions considered in the upscaling procedure. Figure 2 shows two typical examples of the samples employed in the numerical analysis.

With respect to the physical properties to be employed in the numerical simulations, we consider parameters representative of an isotropic tight sandstone for the intact background embedding the fractures (Rubino et al. 2017). In this sense, the solid grains are characterized by a bulk modulus $K_{\rm s}^{\rm b}$=37 GPa and a density $\rho_{\rm s}^{\rm b}$=2650 Kg/m^3. For the dry frame, we use a porosity $\phi^{\rm b}$=0.05, a

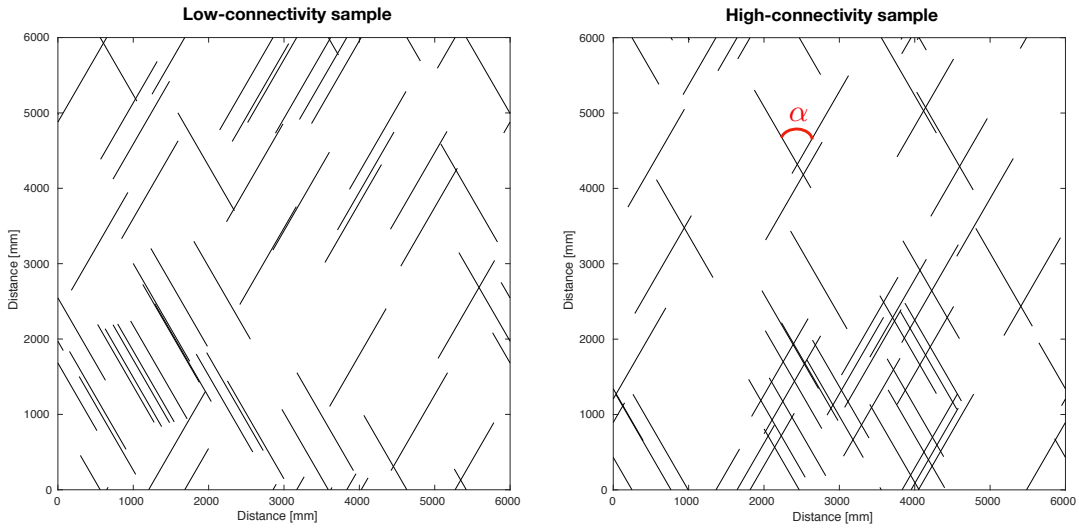

Figure 2. Typical samples employed in the Monte Carlo analysis to compute the reflection coefficients of fractured formations of contrasting degree of interconnectivity. Both samples have 50 fractures and, for this particular example, half of them are inclined -30^o and +30^o with respect to the vertical direction, forming an intersection angle $\alpha = 60^o$. The sample on the left has less than 10 fracture intersections, wheres the one on the right more than 60 intersections.

permeability $\kappa^{\rm b}$=10^{-5} mD, a drained-frame bulk modulus $K^{\rm b}_{\rm m}$=31.5 GPa, and a drained-frame shear modulus $\mu^{\rm b}_{\rm m}$=37.4 GPa. For the fractures, we assume that, at the grain level, the physical properties are the same as those of the background. For the dry-frame properties, we use a bulk modulus $K^{\rm f}_m = 0.04$ GPa and a shear modulus $\mu^{\rm f}_m$= 0.02 GPa, while we set the porosity to $\phi^{\rm f}$=0.8 and the permeability to $\kappa^{\rm f}$=1000 D (Rubino et al. 2017). Both the background and the fractures are saturated with water with a bulk modulus K_w=2.25 GPa, a density ρ_w=1090 Kg/m^3, and a shear viscosity η_w=0.001 Pa $\cdot$ s. The chosen mechanical properties are consistent with a fracture shear compliance $\eta_T = 2.5 \times 10^{-10}$m/Pa, and normal compliances $\eta_N^{dry} = 7.5 \times 10^{-11}$m/Pa and $\eta_N^{undrained} = 1.76 \times 10^{-12}$ m/Pa for the dry and undrained cases, respectively. Overall, these values are in agreement with compliances of meter-scale fractures (Barbosa et al. 2019). On the other hand, the effective elastic properties of the homogeneous region overlying the fractured formation are obtained using Gassmann's equations, considering the previously mentioned physical properties of the intact background.

Since conjugate shear fractures can be associated with a wide range of angles (e.g., Liu & Martinez 2012), we consider 3 different scenarios: α =45^o, 60^o, and 75^o. For each value of α, we randomly generate 40 samples for both the low and high connectivity models and compute the reflection coefficients for a frequency of 30 Hz. The mean values and variances of the resulting coefficients represent

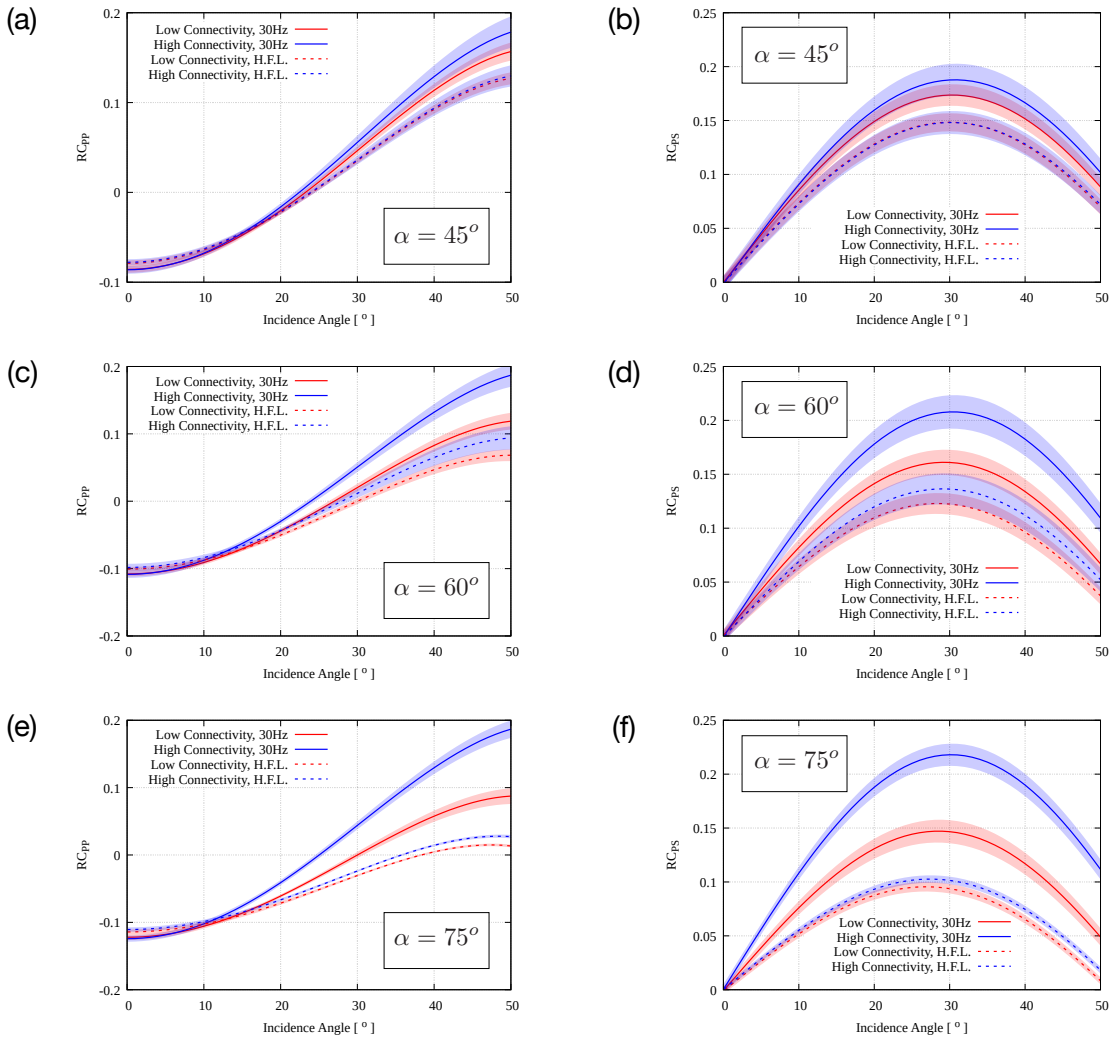

Figure 3. P-wave (left) and S-wave (right) reflection coefficients as a function of incidence angle for a frequency of 30 Hz and a set of fractures characterized by intersection angles α of (a, b) 45^o, (c, d) 60^o and (e, f) 75^o. Red and blue depict the responses of the low- and high-connectivity scenarios, respectively. Thick solid lines denote the average responses, whereas the bounding shaded areas indicate the corresponding standard deviation intervals. Dashed lines denote the high-frequency limit (H.F.L.), or elastic, responses.

the statistical characteristics of the reflectivity of the studied fractured formations. To ensure convergence in terms of the total number of realizations, we compute the standard deviations of the reflection coefficients as a cumulative function of realizations. Convergence is reached when these parameters stabilize at quasi-constant values (Rubino et al. 2009), which is indeed the case for the current study, as shown in Appendix B.

3.2 Results

The left-hand panels of Figure 3 show, for a frequency of 30 Hz, the average P-wave reflection coefficient as a function of incidence angle for the three fracture intersection angles considered. It can be seen that in all cases for incidence angles above $\sim 20^o$ or $\sim 30^o$, the reflection coefficient is higher for the high-connectivity model. The discrepancies increase with both the incidence angle and the fracture intersection angle α. For comparison, we also include the average reflection coefficients in the high-frequency limit (dashed lines), which correspond to the elastic limit, for which FPD effects are absent. We observe that, also in this case, there is a tendency towards increasing reflection coefficients with fracture interconnectivity. However, the sensitivity is much smaller and would be hardly observable in real data. This is expected, since Grechka & Kachanov (2006) showed that the degree of fracture interconnectivity has a negligible effect on the effective seismic response in an elastic context. In addition, these results show that the increase of the reflection coefficients with fracture interconnectivity for a frequency of 30 Hz is mainly due to FPD effects. It is also interesting to notice that, for the low-connectivity models, the reflection coefficients attain higher values than those in the high-frequency limit. This observation suggests that the presence of some connected fractures is sufficient for producing a noticeable effect.

The right-hand panels of Figure 3 show the average S-wave reflection coefficient for an incident P-wave as a function of incidence angle. We observe that, also in this case, the reflection coefficient is sensitive to fracture interconnectivity and that this sensitivity increases with increasing fracture intersection angle. Indeed, clear discrepancies between the responses can be seen, especially for incidence angles above $\sim 10^o$. For instance, for $\alpha = 60^o$ and incidence angles around 30^o, the reflection coefficient for the high-connectivity model is $\sim$0.21, while for the lower degree of interconnectivity it is $\sim$0.16. This shows that, for relatively low incidence angles, the discrepancies between the two scenarios can be significant, thus illustrating that seismic reflection data may be used to assess fracture interconnectivity. In the high-frequency limit, the responses are again not sensitive to interconnectivity.

To understand the reasons for the changes in reflectivity associated with fracture interconnectivity, we show in Table 1 the averages of the effective stiffness matrix components over the considered 40 realizations for a fracture intersection angle $\alpha = 60^o$. We observe that for both low and high connectivity scenarios, $< C_{16}^{\text{eff}} >$ and $< C_{26}^{\text{eff}} >$ are very small, showing that the responses are mainly controlled by $< C_{11}^{\text{eff}} >$, $< C_{22}^{\text{eff}} >$, $< C_{12}^{\text{eff}} >$ and $< C_{66}^{\text{eff}} >$. Moreover, while the values of $< C_{11}^{\text{eff}} >$, $< C_{22}^{\text{eff}} >$, and $< C_{12}^{\text{eff}} >$ do not change significantly with fracture interconnectivity, $< C_{66}^{\text{eff}} >$ was reduced by almost 30% when comparing the low- and high-connectivity scenarios. This means that the change of $< C_{66}^{\text{eff}} >$ with fracture interconnectivity is responsible for the discrepancies observed in the reflection coefficients for the two end-member-type models. Although not shown here for brevity,

Table 1. Average values of the components of the effective stiffness matrix over the considered 40 samples, for a fracture intersection angle $\alpha = 60^o$. We consider both the low and high connectivity models, and a frequency of 30Hz. Please notice that the symbol i denotes the imaginary unit.

	Low Fracture Connectivity [GPa]	**High Fracture Connectivity [GPa]**
$< C_{11}^{\text{eff}} >$	49.27 + 0.13 i	49.78 + 0.25 i
$< C_{22}^{\text{eff}} >$	53.71 + 0.15 i	53.58 + 0.24 i
$< C_{66}^{\text{eff}} >$	18.53 + 1.01 i	12.97 + 0.95 i
$< C_{12}^{\text{eff}} >$	26.88 - 0.07 i	26.77 -0.17 i
$< C_{16}^{\text{eff}} >$	-0.06 - 0.01 i	0.01 i
$< C_{26}^{\text{eff}} >$	-0.04 + 0.01 i	0.1 - 0.01 i

similar behaviours were obtained for the other fracture intersection angles considered in this work. In particular, $< C_{66}^{\text{eff}} >$ was reduced by almost 11% for $\alpha = 45^o$ when comparing the low- and high-connectivity scenarios, whereas this reduction reached a value of 40% in the case of $\alpha = 75^o$. These results also show that the impact of fracture connectivity on $< C_{66}^{\text{eff}} >$ increases with the value of α.

With respect to the physical reasons for the behaviours observed for the stiffness coefficients, it has to be taken into account that in the case of low-permeability formations containing fractures and for typical seismic frequencies, there is not enough time in a half wave cycle for hydraulic communication between the fractures and the background. This implies that the fractures behave as hydraulically sealed with respect to the background (Rubino et al. 2014). Therefore, when a seismic wave compresses a disconnected fracture, it increases its fluid pressure, counteracting the associated deformation of the fracture. This is referred to as the stiffening effect of the fracture fluid. However, in the presence of connected fractures of different orientations, there is enough time for the fluid pressure within the fractures to relax due to their typically very high permeabilities (Rubino et al. 2014). Therefore, the stiffening effect of the fluid saturating connected fractures diminishes in comparison with the corresponding unconnected case and, hence, can alter the effective stiffness coefficients. While this effect does not have a significant impact on $< C_{11}^{\text{eff}} >$, $< C_{22}^{\text{eff}} >$, and $< C_{12}^{\text{eff}} >$ for the considered models, it alters significantly the value of $< C_{66}^{\text{eff}} >$. This can be understood by analyzing the following situations. When a simple shear test is applied to a sample containing unconnected conjugate fractures, the fractures are strongly deformed. Since they behave as hydraulically sealed, high absolute values of fluid pressure inside both fractures sets arise, thus counteracting the deformation and increasing the overall rigidity. Due to the opposite orientations of the two fracture sets, there is an

increase of pressure in one of the fracture sets, while the pressure decreases in the other one (Rubino et al. 2017). Consequently, if these fractures are connected, the resulting pressure gradient triggers fracture-to-fracture FPD, reducing the magnitude of the fluid pressure inside the connected fractures, which diminishes the overall rigidity of the formation. This explains the drop of the value of $< C_{66}^{\text{eff}} >$ for the high-connectivity models. On the other hand, in the case of an oscillatory horizontal or vertical compression, the fluid pressure increases (or decreases) in all fracture and, therefore, the resulting FPD in the presence of connected fractures is largely negligible. This implies that the stiffening effect of the fracture fluid is not significantly affected by FPD and, therefore, $< C_{11}^{\text{eff}} >$, $< C_{22}^{\text{eff}} >$, and $< C_{12}^{\text{eff}} >$ remain rather unaltered when comparing the two end-member-type models. The numerical results also show that this poroelastic effect tends to increase with the intersection angle α. This is due to the fact that as α increases, and as long as its value is below 90^o, the fluid pressure gradient generated between the conjugate fractures in response to a shear perturbation tends to increase. Indeed, the maximum discrepancies between the responses of the end-member-type models are expected to arise for $\alpha = 90^o$. It is important to remark here that these results are strictly valid for conjugate fracture sets equally inclined with respect to the vertical. Additional numerical simulations would be needed to explore other scenarios, which will be considered in future works.

Another interesting aspect of the stiffness components shown in Table 1 and those obtained for $\alpha = 45^o$ and 75^o is that their imaginary parts get very low values in comparison with the corresponding real parts. This, in other words, implies that for the considered frequency, the effective response of the fractured formation is essentially elastic, that is, seismic attenuation and velocity dispersion are negligible. This is due to the fact that, for the seismic frequency band, the pore fluid is in relaxed state inside the fractures and in the unrelaxed state in the embedding porous background. Consequently, there is no energy dissipation associated with pore fluid movement for such frequencies. This implies that the fracture interconnectivity effects are not manifested as seismic attenuation or dispersion for the considered frequencies, but in the form of variations of the compliance of connected fractures. For frequencies well below and well above the seismic frequency band, seismic attenuation and dispersion due to fracture-background and fracture-fracture FPD, respectively, are expected to arise (Rubino et al. 2014).

3.3 Impact on AVA coefficients

For a seismic profile perpendicular to the azimuth of the fractures, the P-wave reflection coefficient can be approximated by (Liu & Martinez 2012)

$$RC_{pp}(\theta) = A + B\sin(\theta)^2 + C\sin(\theta)^4, \tag{6}$$

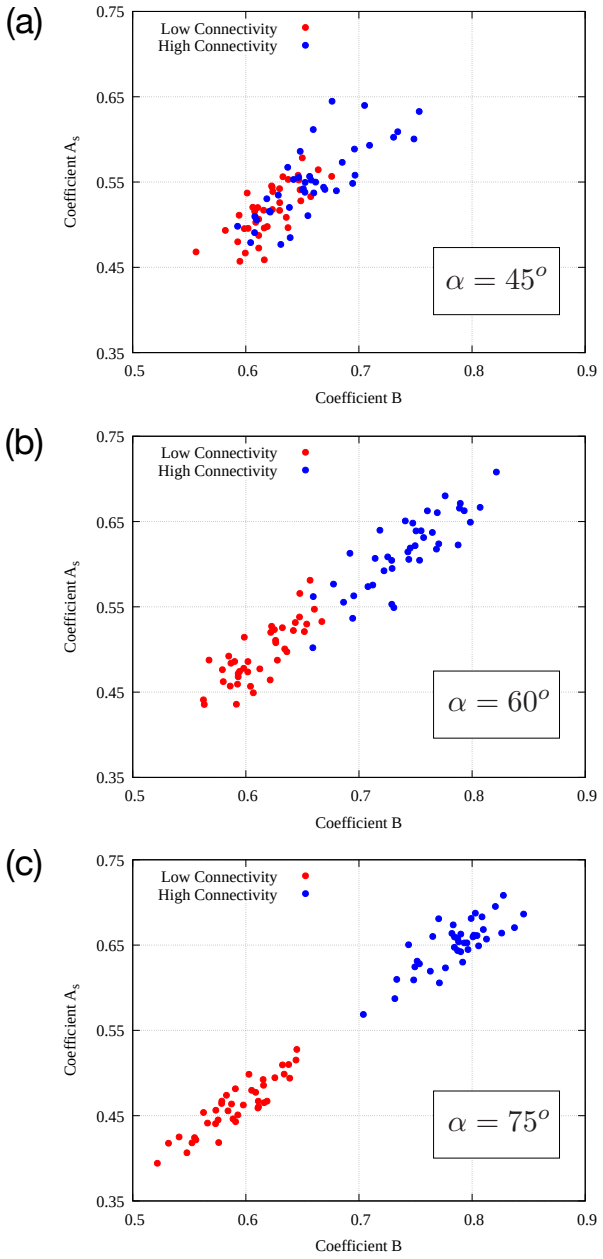

Figure 4. Crossplot of AVA coefficients B and A_s (eqs. 6 and 7) for fracture intersection angles α of 45^o, 60^o, and 75 ^{o}. Red and blue color denotes the results for the low- and high-connectivity scenarios, respectively.

where the AVA coefficients A, B, and C are referred to as the intercept, the gradient, and the curvature, respectively. In the case of the S-wave reflection coefficient, the following approximation can be used (Liu & Martinez 2012)

$$RC_{ps}(\theta) = A_S \sin(\theta) + B_S \sin(\theta)^3, \tag{7}$$

where A_S and B_S are referred to as the near- and far-offset responses, respectively. These coefficients are commonly extracted from seismic data and employed to provide fluid and lithology information (e.g., Rüger 2002).

In order to explore the impact of the FPD effects related to fracture interconnectivity on these AVA parameters, we determine, for each sample considered in this work, the set of parameters that produces the best fit of the corresponding reflectivity curves with eqs. 6 and 7. Please notice that we use the responses of the individual samples before averaging, to account for possible perturbations of the AVA coefficients related to slight variations of fracture interconnectivity and interactions. This analysis allows to verify that, while there are no significant differences in the values of A and C when comparing different fracture interconnectivities, the other AVA parameters show measurable changes. Indeed, we observe in a crossplot of coefficients B and A_s that, while in the case of $\alpha = 45^o$ there is an overlap between the clusters for low and high fracture interconnectivity, the clusters are clearly separated for $\alpha = 60^o$ and 75^o (Figure 4). In the latter cases, higher values of the coefficients B and A_S are associated with higher degrees of fracture interconnectivity. These results therefore suggest that for $\alpha \geq 60^o$, these AVA coefficients could be used to delineate the regions of the probed formation associated with higher or lower fracture interconnectivity. In this context it is important, however, to take into account that when analyzing real seismic data to infer fracture interconnectivity, uncertainties in the input parameters as well as errors in the data will inherently be present. Moreover, the fractures are expected to be finite in the third dimension and their presence will give rise to azimuthal anisotropy. These topics will be explored in future works.

4 CONCLUSIONS

In this work, we have computed seismic reflection coefficients at the top of a fractured formation, considering sets of conjugate fractures characterized by different orientations and degrees of interconnectivity. The effective elastic properties of the probed formations were determined in a poroelastic framework that accounts for the effects of FPD between fractures and background as well as within connected fractures. Our analysis demonstrates for the first time that the reflection coefficients are sensitive to the degree of interconnectivity of the probed fracture network which, in turn, implies that this key information can be retrieved from seismic data. Moreover, our results suggest that commonly employed AVA coefficients can help to delineate the regions of a fractured network characterized by higher interconnectivity. This previously unknown sensitivity of seismic reflectivity to fracture interconnectivity is related to variations of the stiffening effect of the fluid contained within connected fractures due to wave-induced FPD, a physical process that should be accounted for when assessing the AVA response of these media.

DATA AVAILABILITY

The data associated with this paper are available at https://doi.org/10.5281/zenodo.5645687.

REFERENCES

Ali, A. & Jakobsen, M., 2014. Anisotropic permeability in fractured reservoirs from frequency-dependent seismic amplitude versus angle and azimuth data, *Geophysical prospecting*, **62**(2), 293–314.

Bakulin, A., Grechka, V., & Tsvankin, I., 2000. Estimation of fracture parameters from reflection seismic datapart ii: Fractured models with orthorhombic symmetry, *Geophysics*, **65**(6), 1803–1817.

Barbosa, N. D., Caspari, E., Rubino, J. G., Greenwood, A., Baron, L., & Holliger, K., 2019. Estimation of fracture compliance from attenuation and velocity analysis of full-waveform sonic log data, *Journal of Geophysical Research: Solid Earth*, **124**, 2738–2761.

Barton, N., 2006. *Rock quality, seismic velocity, attenuation and anisotropy*, Taylor and Francis Group, London.

Berkowitz, B., Bour, O., Davy, P., & Odling, N., 2000. Scaling of fracture connectivity in geological formations, *Geophysical Research Letters*, **27**, 2061–2064.

Biot, M. A., 1941. General theory of three-dimensional consolidation, *Journal of Applied Physics*, **12**, 155–164.

Biot, M. A., 1962. Mechanics of deformation and acoustic propagation in porous media, *Journal of Applied Physics*, **33**, 1482–1498.

Boadu, F. K., 2000. Predicting the transport properties of fractured rocks from seismic information: numerical experiments, *Journal of Applied Geophysics*, **44**, 103–113.

Carcione, J., 1997. Reflection and transmission of qp-qs plane waves at a plane boundary between viscoelastic transversely isotropic media, *Geophysics*, **129**, 669–680.

Carcione, J., 2007. *Wave fields in real media: Wave propagation in anisotropic, anelastic, porous and electromagnetic media*, Elsevier, Amsterdam.

Chapman, M., 2009. Modeling the effect of multiple sets of mesoscale fractures in porous rocks on frequency-dependent anisotropy, *Geophysics*, **74**, D97–D103.

Favino, M., Hunziker, J., Caspari, E., Quintal, B., Holliger, K., & Krause, R., 2020. Fully-automated adaptive mesh refinement for media embedding complex heterogeneities: Application to poroelastic fluid pressure diffusion, *Computational Geosciences*, **24**, 1101–1120.

Galvin, R. J., Gurevich, B., & Sayers, C. M., 2007. Fluid-dependent shear-wave splitting in a poroelastic medium with conjugate fracture sets, *Geophys. Prospect.*, **55**, 333–343.

Grechka, V. & Kachanov, M., 2006. Effective elasticity of rocks with closely spaced and intersecting cracks, *Geophysics*, **71**, D85–D91.

Guo, J., Rubino, J. G., Barbosa, N. D., Glubokovskikh, S., & Gurevich, B., 2018. Seismic dispersion and atten-

uation in saturated porous rocks with aligned fractures of finite thickness: Theory and numerical simulations - Part I: P-wave perpendicular to the fracture plane, *Geophysics*, **83**, WA49–WA62.

Hunziker, J., Favino, M., Caspari, E., Quintal, B., Rubino, J. G., Krause, R., & Holliger, K., 2018. Seismic attenuation and stiffness modulus dispersion in porous rocks containing stochastic fracture networks, *Journal of Geophysical Research*, **123**, 125–143.

Jakobsen, M., Liu, E., & Chapman, M., 2007. Estimation of anisotropic permeability in fractured reservoirs from seismic avoz analysis, in *SEG Technical Program Expanded Abstracts 2007*, pp. 99–103, Society of Exploration Geophysicists.

Liu, E. & Martinez, A., 2012. *Seismic fracture characterization: Concepts and practical applications*, European Association of Geoscientists & Engineers.

Liu, E., Hudson, J. A., & Pointer, T., 2000. Equivalent medium representation of fractured rock, *Journal of Geophysical Research*, **105**, 2981–3000.

Maultzsch, S., Chapman, M., Liu, E., & Li, X. Y., 2003. Modelling frequency-dependent seismic anisotropy in fluid-saturated rock with aligned fractures: Implication of fracture size estimation from anisotropic measurements, *Geophysical Prospecting*, **51**, 381–392.

Mavko, G., Mukerji, T., & Dvorkin, J., 1998. *The rock physics handbook: Tools for seismic analysis in porous media*, Cambridge University Press.

Nelson, R., 2001. *Geologic Analysis of Naturally Fractured Reservoirs. Second Edition*, Gulf Professional Publishing.

Rubino, J. G., Ravazzoli, C. L., & Santos, J. E., 2009. Equivalent viscoelastic solids for heterogeneous fluid-saturated porous rocks, *Geophysics*, **74**, N1–N13.

Rubino, J. G., Guarracino, L., Müller, T. M., & Holliger, K., 2013. Do seismic waves sense fracture connectivity?, *Geophysical Research Letters*, **40**, 692–696.

Rubino, J. G., Müller, T. M., Guarracino, L., Milani, M., & Holliger, K., 2014. Seismoacoustic signatures of fracture connectivity, *Journal of Geophysical Research*, **119**, 2252–2271.

Rubino, J. G., Caspari, E., Müller, T. M., Milani, M., Barbosa, N., & Holliger, K., 2016. Numerical upscaling in 2D heterogeneous poroelastic rocks: Anisotropic attenuation and dispersion of seismic waves, *Journal of Geophysical Research*, **121**, 6698–6721.

Rubino, J. G., Caspari, E., Müller, T. M., & Holliger, K., 2017. Fracture connectivity can reduce the velocity anisotropy of seismic waves, *Geophysical Journal International*, **210**, 223–227.

Rüger, A., 2002. *Reflection coefficients and azimuthal AVO analysis in anisotropic media*, Society of Exploration Geophysicists.

APPENDIX A: MATHEMATICAL DERIVATION OF THE PROCEDURE FOR OBTAINING THE SCATTERING COEFFICIENTS

A1 Plane waves in homogeneous, generically-anisotropic, viscoelastic media

We first consider the propagation of plane waves in a homogeneous, generically-anisotropic 2D medium. In particular, we analyse propagation in the $x-y$ plane under plane strain conditions, such that the wave equation in the space-frequency domain can be written as

$$-\omega^2\rho u_1 - \frac{\partial\sigma_{11}}{\partial x} - \frac{\partial\sigma_{12}}{\partial y} = 0, \tag{A.1}$$

$$-\omega^2\rho u_2 - \frac{\partial\sigma_{12}}{\partial x} - \frac{\partial\sigma_{22}}{\partial y} = 0, \tag{A.2}$$

where ω is the angular frequency, ρ the mass density of the medium, $\boldsymbol{u} = (u_1, u_2)$ the particle displacement vector, and $\boldsymbol{\sigma}$ the stress tensor. These equations are coupled through the stress-strain relations, which in the considered generically-anisotropic case can be written as

$$\begin{pmatrix} \sigma_{11} \\ \sigma_{22} \\ \sigma_{12} \end{pmatrix} = \begin{pmatrix} C_{11} & C_{12} & C_{16} \\ C_{12} & C_{22} & C_{26} \\ C_{16} & C_{26} & C_{66} \end{pmatrix} \begin{pmatrix} \epsilon_{11} \\ \epsilon_{22} \\ 2\epsilon_{12} \end{pmatrix}, \tag{A.3}$$

where $\boldsymbol{\epsilon} = (\epsilon_{ij})$ is the strain tensor and $\boldsymbol{C} = (C_{ij})$ is the stiffness matrix. The elements C_{ij} can be complex-valued and frequency-dependent to take into account viscoelastic behaviour of the material.

Let us now consider a plane wave of frequency ω propagating through a medium characterized by the stiffness matrix $\boldsymbol{C}$. As the associated displacement field is not necessarily polarized in the direction of propagation or transverse to it, it is convenient to express the horizontal and vertical displacements in the space-frequency domain as

$$u_1 = Ae^{-i\boldsymbol{k}\cdot\boldsymbol{x}}, \tag{A.4}$$

$$u_2 = Be^{-i\boldsymbol{k}\cdot\boldsymbol{x}}, \tag{A.5}$$

where $\boldsymbol{k} = (n, l)$ is the wave vector, $\boldsymbol{x}$ the position, and the complex-valued scalars A and B are the amplitudes of the horizontal and vertical displacements, respectively. In the most general case, the seismic wave can be inhomogeneous, that is, the propagation vector is not parallel to the attenuation vector. For this reason, we express the wave vector as

$$\boldsymbol{k} = \boldsymbol{k_R} - i\boldsymbol{k_{Im}}, \tag{A.6}$$

where the vectors $\boldsymbol{k_R}$ and $\boldsymbol{k_{Im}}$ are real-valued and, while the former points in the direction normal to the planes of constant phase, the latter is oriented in a direction normal to planes of constant amplitude.

Introducing the equalities A.3 in the equations A.1-A.2 and using the relations A.4-A.5 , we get

the following system of equations

$$\left[-\omega^2\rho + C_{11}n^2 + 2C_{16}nl + C_{66}l^2\right] A + \left[C_{16}n^2 + (C_{12}+C_{66})\,nl + C_{26}l^2\right] B = 0, \quad \text{(A.7)}$$

$$\left[C_{16}n^2 + (C_{12}+C_{66})\,nl + C_{26}l^2\right] A + \left[-\omega^2\rho + C_{66}n^2 + 2C_{26}nl + C_{22}l^2\right] B = 0. \quad \text{(A.8)}$$

To obtain non-trivial solutions for A and B, the determinant of the linear system of equations A.7-A.8 has to be zero. Imposing this condition, we get

$$Pl^4 + Ql^3 + Rl^2 + Sl + T = 0, \quad \text{(A.9)}$$

with

$$P = C_{22}C_{66} - C_{26}^2, \quad \text{(A.10)}$$

$$Q = 2n\left(C_{16}C_{22} - C_{12}C_{26}\right), \quad \text{(A.11)}$$

$$R = n^2\left(C_{11}C_{22} + 2C_{16}C_{26} - C_{12}^2 - 2C_{12}C_{66}\right) - \omega^2\rho\left(C_{22}+C_{66}\right), \quad \text{(A.12)}$$

$$S = 2n^3\left(C_{11}C_{26} - C_{16}C_{12}\right) - 2\omega^2\rho n\left(C_{16}+C_{26}\right), \quad \text{(A.13)}$$

$$T = n^4\left(C_{11}C_{66} - C_{16}^2\right) - \omega^2 n^2\rho\left(C_{11}+C_{66}\right) + \omega^4\rho^2. \quad \text{(A.14)}$$

Equation A.9 is the dispersion relation and, given the properties of the medium and the horizontal component of the wave vector n, it allows to determine the plausible values for its vertical component l. Equation A.9 has four solutions, which correspond to the quasi-compressional and quasi-shear waves traveling upwards and downwards in the medium. To decide whether one of the solutions corresponds to a wave traveling upwards or downwards, we must compute the Umov-Poynting vector and determine the direction in which the energy propagates.

According to equation A.7, the relationship between the amplitudes A and B can be written as

$$A = \gamma B, \quad \text{(A.15)}$$

with

$$\gamma = \frac{-C_{16}n^2 - (C_{12}+C_{66})nl - C_{26}l^2}{-\omega^2\rho + C_{11}n^2 + 2C_{16}nl + C_{66}l^2}. \quad \text{(A.16)}$$

In the seismic reflection problem addressed in this work, we consider a P-wave incident on a fractured formation having an effective velocity lower than that of the overlying medium. In this scenario, the involved reflected and transmitted waves will have propagation directions relatively far from the horizontal. Thus, for the P-waves involved in this work, equation A.15 can be used without producing numerical issues since $||B|| >> 0$. Conversely, numerical problems could arise for S-waves traveling in a direction close to the vertical axis. For instance, if a plane S-wave travels vertically in a HTI medium, $B = 0$ and $\gamma \to \infty$. To avoid this potential problem in the case of the S-waves involved in

this work, we express the relationship between the displacement amplitudes through

$$B = \beta A, \tag{A.17}$$

with

$$\beta = \frac{-\omega^2\rho + C_{11}n^2 + 2C_{16}nl + C_{66}l^2}{-C_{16}n^2 - (C_{12} + C_{66})nl - C_{26}l^2}. \tag{A.18}$$

When seismic waves propagate through anisotropic media, the direction in which the associated energy travels does not necessarily coincide with the propagation direction (Carcione 2007). For this reason, it is important to compute the Umov-Poynting vector, which quantifies the magnitude and direction of the power flow associated with the seismic perturbation. The *complex Umov-Poynting vector* is given by (Carcione 2007)

$$\boldsymbol{P} = -\frac{1}{2}\boldsymbol{\Sigma} \cdot \boldsymbol{v}^*, \tag{A.19}$$

where, in the considered 2D case,

$$\boldsymbol{\Sigma} = \begin{pmatrix} \sigma_{11} & \sigma_{12} \\ \sigma_{12} & \sigma_{22} \end{pmatrix}, \tag{A.20}$$

and $\boldsymbol{v}^* = -i\omega\boldsymbol{u}^*$ is the complex conjugate of the particle velocity. The time-average of the *real Umov-Poytning vector* $\boldsymbol{P_R}$ represents the magnitude and direction of the time-averaged power flow, and satisfies $< \boldsymbol{P_R} >= \Re(\boldsymbol{P})$ (Carcione 2007). Therefore, to determine whether a given wave travels upwards or downwards, we need to examine the real part $\Re$ of the vertical component of the complex Umov-Poytning vector. Using the expressions of the solid displacement in terms of the amplitudes A and B, and the stress-strain relations, it is straightforward to show that the vertical component of $\boldsymbol{P}$ can be expressed as

$$P_2 = \frac{\omega}{2}\Big[(C_{16}n + C_{66}l)\,||A||^2 + (C_{26}l + C_{66}n)\,A^*B + \tag{A.21}$$
$$(C_{12}n + C_{26}l)\,AB^* + (C_{22}l + C_{26}n)\,||B||^2\Big].$$

For P-waves, expressing A in terms of B, this equation can be written as

$$P_2 = \frac{\omega||B||^2}{2}\Big[(C_{16}n + C_{66}l)\,||\gamma||^2 + (C_{26}l + C_{66}n)\,\gamma^* + \tag{A.22}$$
$$(C_{12}n + C_{26}l)\,\gamma + C_{22}l + C_{26}n\Big].$$

Since $\omega||B||^2/2 \geq 0$, the sign of

$$\Re\Big[(C_{16}n + C_{66}l)\,||\gamma||^2 + (C_{26}l + C_{66}n)\,\gamma^* + \tag{A.23}$$
$$(C_{12}n + C_{26}l)\,\gamma + C_{22}l + C_{26}n\Big],$$

determines whether a given P-wave travels upwards or downwards. In the case of S-waves, following

a similar procedure and expressing B in terms of A, it can be shown that the direction of propagation is given by the sign of

$$\Re\Big[C_{16}n + C_{66}l + (C_{26}l + C_{66}n)\,\beta + (C_{12}n + C_{26}l)\,\beta^* + (C_{22}l + C_{26}n)\,||\beta||^2\Big]. \tag{A.24}$$

A2 Scattering coefficients at a plane interface

Let us consider a plane interface at $y = 0$ separating two halfspaces Ω_U and Ω_L (Figure 1), with the y-axis pointing downwards. A plane homogeneous P-wave arrives at the interface from Ω_U with an angle θ measured with respect to its normal. This perturbation generates four waves at the interface: reflected and transmitted quasi-P- and quasi-S-waves.

A2.1 Incident wave

We assume that the incident wave is compressional and homogeneous. Thus, the components of the wave vector can be expressed as

$$n = k_I \sin\theta, \tag{A.25}$$

$$l_I = k_I \cos\theta, \tag{A.26}$$

where k_I is the wavenumber and θ the incidence angle. Using these expressions in equations A.9-A.14, we get

$$U k_I^4 + V k_I^2 + W = 0, \tag{A.27}$$

with

$$\begin{aligned} U &= (C_{11}^U C_{66}^U - (C_{16}^U)^2)\sin\theta^4 + 2(C_{11}^U C_{26}^U - C_{16}^U C_{12}^U)\sin\theta^3\cos\theta + \\ &\quad (C_{11}^U C_{22}^U + 2C_{16}^U C_{26}^U - (C_{12}^U)^2 - 2C_{12}^U C_{66}^U)\sin\theta^2\cos\theta^2 + \\ &\quad 2(C_{16}^U C_{22}^U - C_{12}^U C_{26}^U)\sin\theta\cos\theta^3 + (C_{22}^U C_{66}^U - (C_{26}^U)^2)\cos\theta^4 \end{aligned} \tag{A.28}$$

$$\begin{aligned} V &= -\omega^2\rho_U(C_{11}^U + C_{66}^U)\sin\theta^2 - 2\omega^2\rho_U(C_{16}^U + C_{26}^U)\sin\theta\cos\theta - \\ &\quad \omega^2\rho_U(C_{22}^U + C_{66}^U)\cos\theta^2 \end{aligned} \tag{A.29}$$

$$W = \omega^4\rho_U^2, \tag{A.30}$$

where, from now on, the super- and subscript U denote the value of any variable in Ω_U. Equation A.27 is a biquadratic polynomial, whose four roots correspond to a quasi-P- and a quasi-S-wave traveling upwards and another pair of quasi-P- and quasi-S-waves traveling downwards. The different types of

waves can be identified computing their phase velocities (Carcione 2007)

$$\boldsymbol{V} = \frac{\omega}{k_R}\hat{\boldsymbol{k}}_{\boldsymbol{R}}, \tag{A.31}$$

where k_R is the modulus of $\boldsymbol{k_R}$ and $\hat{\boldsymbol{k}}_{\boldsymbol{R}}$ its normalized vector.

From the two resulting wavenumbers associated with quasi-P-waves, we choose the one that corresponds to a wave traveling downwards, that is, the wavenumber for which expression A.23 assumes a value grater than zero. Like this, we determine the wavenumber k_I of the incident wave and, using equations A.25 and A.26 , the corresponding horizontal and vertical components, n and l_I.

A2.2 Wavefields in the upper medium

The displacement field $\boldsymbol{u^I}$ associated with the incident wave can be written as

$$u_1^I = \gamma_I B_I e^{-i(nx+l_I y)}, \tag{A.32}$$

$$u_2^I = B_I e^{-i(nx+l_I y)}. \tag{A.33}$$

For the reflected waves, using the superposition principle, the associated displacement field is

$$u_1^r = u_1^{rp} + u_1^{rs}, \tag{A.34}$$

$$u_2^r = u_2^{rp} + u_2^{rs}, \tag{A.35}$$

where $\boldsymbol{u^{rp}}$ and $\boldsymbol{u^{rs}}$ are the contributions of the reflected quasi-P- and quasi-S-waves. Therefore,

$$u_1^r = \gamma_{pr} B_{pr} e^{-i(nx+l_p^r y)} + A_{sr} e^{-i(nx+l_s^r y)}, \tag{A.36}$$

$$u_2^r = B_{pr} e^{-i(nx+l_p^r y)} + \beta_{sr} A_{sr} e^{-i(nx+l_s^r y)}. \tag{A.37}$$

In these equations, we make use of Snell's law, which indicates that the horizontal component of the wave vector of the reflected waves is equal to that of the incident wave n. On the other hand, the vertical components of the wave vectors of the reflected P- and S-waves, l_p^r and l_s^r, are obtained by solving equation A.9 and choosing the corresponding roots, for which expressions A.23 and A.24, respectively, assume negative values.

Employing the superposition principle, the displacement field in Ω_U can thus be expressed by

$$u_1^U = \gamma_I B_I e^{-i(nx+l_I y)} + \gamma_{pr} B_{pr} e^{-i(nx+l_p^r y)} + A_{sr} e^{-i(nx+l_s^r y)}, \tag{A.38}$$

$$u_2^U = B_I e^{-i(nx+l_I y)} + B_{pr} e^{-i(nx+l_p^r y)} + \beta_{sr} A_{sr} e^{-i(nx+l_s^r y)}. \tag{A.39}$$

Using these expressions to compute the components of the strain tensor and employing the resulting expressions in the stress-strain relations (equation A.3), we evaluate the components σ_{22}^U and σ_{12}^U of

the stress tensor at the interface $y = 0$

$$\sigma_{22}^U(x,0) = -ie^{-inx}\Big\{\left[C_{12}^U n\gamma_I + C_{22}^U l_I + C_{26}^U(l_I\gamma_I + n)\right]B_I + \left[C_{12}^U n\gamma_{pr} + C_{22}^U l_p^r + C_{26}^U(l_p^r\gamma_{pr} + n)\right]B_{pr} + \left[C_{12}^U n + C_{22}^U l_s^r\beta_{sr} + C_{26}^U(l_s^r + n\beta_{sr})\right]A_{sr}\Big\}, \tag{A.40}$$

$$\sigma_{12}^U(x,0) = -ie^{-inx}\Big\{\left[C_{16}^U n\gamma_I + C_{26}^U l_I + C_{66}^U(l_I\gamma_I + n)\right]B_I + \left[C_{16}^U n\gamma_{pr} + C_{26}^U l_p^r + C_{66}^U(l_p^r\gamma_{pr} + n)\right]B_{pr} + \left[C_{16}^U n + C_{26}^U l_s^r\beta_{sr} + C_{66}^U(l_s^r + n\beta_{sr})\right]A_{sr}\Big\}. \tag{A.41}$$

A2.3 Wavefields in the lower medium

In the lower halfspace, the displacement field is given by

$$u_1^L = u_1^{tp} + u_1^{ts}, \tag{A.42}$$

$$u_2^L = u_2^{tp} + u_2^{ts}, \tag{A.43}$$

where $\boldsymbol{u^{tp}}$ and $\boldsymbol{u^{ts}}$ are the contributions of the transmitted quasi-P- and quasi-S-waves. Please note that, from now on, the super- and subscript L denote the value of any variable in Ω_L. Employing the general plane-wave solution for the particle displacements, we can write

$$u_1^L = \left[\gamma_{pt}B_{pt}e^{-i(nx+l_p^t y)} + A_{st}e^{-i(nx+l_s^t y)}\right], \tag{A.44}$$

$$u_2^L = \left[B_{pt}e^{-i(nx+l_p^t y)} + \beta_{st}A_{st}e^{-i(nx+l_s^t y)}\right]. \tag{A.45}$$

In these expressions, we again make use of Snell's law, that is, the horizontal components of the wave vectors of the transmitted waves are equal to that of the incident wave n. The vertical components, on the other hand, are obtained by solving equation A.9 and choosing the roots associated with quasi-P- and quasi-S-waves for which expressions A.23 and A.24, respectively, assume positive values.

Following similar steps as before, the components of the stress tensor for the lower halfspace computed at the interface can be expressed as

$$\sigma_{22}^L(x,0) = -ie^{-inx}\Big\{\left[C_{12}^L n\gamma_{pt} + C_{22}^L l_p^t + C_{26}^L(l_p^t\gamma_{pt} + n)\right]B_{pt} + \left[C_{12}^L n + C_{22}^L l_s^t\beta_{st} + C_{26}^L(l_s^t + n\beta_{st})\right]A_{st}\Big\}, \tag{A.46}$$

$$\sigma_{12}^L(x,0) = -ie^{-inx}\Big\{\left[C_{16}^L n\gamma_{pt} + C_{26}^L l_p^t + C_{66}^L(l_p^t\gamma_{pt} + n)\right]B_{pt} + \left[C_{16}^L n + C_{26}^L l_s^t\beta_{st} + C_{66}^L(l_s^t + n\beta_{st})\right]A_{st}\Big\}. \tag{A.47}$$

A2.4 Continuity conditions and the reflection and transmission coefficients

The natural boundary conditions at the interface $y = 0$ are the continuity of the displacements and of the stress components σ_{22} and σ_{12}. Imposing these conditions, we get the following linear system of equations, in which the unknown are the displacement amplitudes

$$\gamma_{pr}B_{pr} + A_{sr} - \gamma_{pt}B_{pt} - A_{st} = -\gamma_I B_I, \tag{A.48}$$

$$B_{pr} + \beta_{sr}A_{sr} - B_{pt} - \beta_{st}A_{st} = -B_I, \tag{A.49}$$

$$\begin{aligned}&\left[C_{12}^U n\gamma_{pr} + C_{22}^U l_p^r + C_{26}^U(l_p^r\gamma_{pr} + n)\right] B_{pr} + \left[C_{12}^U n + C_{22}^U l_s^r\beta_{sr} + C_{26}^U(l_s^r + n\beta_{sr})\right] A_{sr} - \\ &\left[C_{12}^L n\gamma_{pt} + C_{22}^L l_p^t + C_{26}^L(l_p^t\gamma_{pt} + n)\right] B_{pt} - \left[C_{12}^L n + C_{22}^L l_s^t\beta_{st} + C_{26}^L(l_s^t + n\beta_{st})\right] A_{st} = \\ &\qquad - \left[C_{12}^U n\gamma_I + C_{22}^U l_I + C_{26}^U(l_I\gamma_I + n)\right] B_I,\end{aligned} \tag{A.50}$$

$$\begin{aligned}&\left[C_{16}^U n\gamma_{pr} + C_{26}^U l_p^r + C_{66}^U(l_p^r\gamma_{pr} + n)\right] B_{pr} + \left[C_{16}^U n + C_{26}^U l_s^r\beta_{sr} + C_{66}^U(l_s^r + n\beta_{sr})\right] A_{sr} - \\ &\left[C_{16}^L n\gamma_{pt} + C_{26}^L l_p^t + C_{66}^L(l_p^t\gamma_{pt} + n)\right] B_{pt} - \left[C_{16}^L n + C_{26}^L l_s^t\beta_{st} + C_{66}^L(l_s^t + n\beta_{st})\right] A_{st} = \\ &\qquad - \left[C_{16}^U n\gamma_I + C_{26}^U l_I + C_{66}^U(l_I\gamma_I + n)\right] B_I.\end{aligned} \tag{A.51}$$

This set of equations allows us to obtain the displacement amplitudes B_{pr}, A_{sr}, B_{pt}, and A_{st} which, in turn, can be used to determine the reflection and transmission coefficients.

In the analyses performed in this work, we consider that the upper medium is elastic and isotropic. In this particular case, we can define the reflection and transmission coefficients in terms of the particle displacements measured with respect to the direction of wave propagation (Mavko et al. 1998). In order to do this, we write the displacement of the incident wave as

$$\boldsymbol{u^I} = C_I\boldsymbol{V_I}, \tag{A.52}$$

where

$$\boldsymbol{V_I} = \left(\frac{\gamma_I}{\sqrt{1+\gamma_I^2}}, \frac{1}{\sqrt{1+\gamma_I^2}}\right)^T, \tag{A.53}$$

is a unit vector parallel to the direction of wave propagation, and

$$C_I = B_I\sqrt{1+\gamma_I^2}. \tag{A.54}$$

Similarly, for the reflected P-wave we can write the associated particle displacement as

$$\boldsymbol{u^{rp}} = C_{rp}\boldsymbol{V_{rp}}, \tag{A.55}$$

with

$$\boldsymbol{V_{rp}} = \left(\frac{-\gamma_{pr}}{\sqrt{1+\gamma_{pr}^2}}, \frac{-1}{\sqrt{1+\gamma_{pr}^2}} \right)^T, \tag{A.56}$$

being a unit vector in the direction of the reflected P-wave, and

$$C_{rp} = -\sqrt{1+\gamma_{pr}^2} B_{pr}. \tag{A.57}$$

Analogously, the particle displacement associated with the reflected S-wave can be expressed as

$$\boldsymbol{u^{rs}} = C_{rs} \boldsymbol{V_{rs}}, \tag{A.58}$$

with

$$\boldsymbol{V_{rs}} = \left(\frac{1}{\sqrt{1+\beta_{sr}^2}}, \frac{\beta_{sr}}{\sqrt{1+\beta_{sr}^2}} \right)^T, \tag{A.59}$$

$$C_{rs} = \sqrt{1+\beta_{sr}^2} A_{sr}. \tag{A.60}$$

We then define the reflection coefficients as the ratio of the particle displacement of the reflected wave measured with respect to the direction of propagation and that corresponding to the incident wave: $RC_{pp} = C_{rp}/C_I$ and $RC_{ps} = C_{rs}/C_I$. Using the expressions given by equations A.54, A.57 and A.60, we get

$$RC_{pp}(\omega, \theta) = -\frac{B_{pr}}{B_I}, \tag{A.61}$$

$$RC_{ps}(\omega, \theta) = \frac{\sqrt{1+\beta_{sr}^2}\, A_{sr}}{\sqrt{1+\gamma_I^2}\, B_I}. \tag{A.62}$$

These are the equations employed in this work to compute the reflection coefficients.

A3 Comparison of the proposed methodology with an analytical solution in the case of an HTI viscoelastic formation

In order to provide an analysis on the correctness of the implementation of the proposed methodology, we compare the reflection coefficients computed using the proposed methodology with those based on an analytical solution for an HTI viscoelastic formation (Carcione 1997). In particular, we consider the reflectivity problem at an interface separating an isotropic elastic overburden and an underlying anisotropic viscoelastic halfspace. We assume that the latter corresponds to a fractured formation and compare the reflection coefficients in the plane perpendicular to the strike of the fractures.

The complex-valued, frequency-dependent stiffness coefficients of the anisotropic medium are computed based on equation 12 of the model of Guo et al. (2018) for a random distribution of planar fractures embedded in a fluid-saturated porous background. For the latter, we consider for the solid

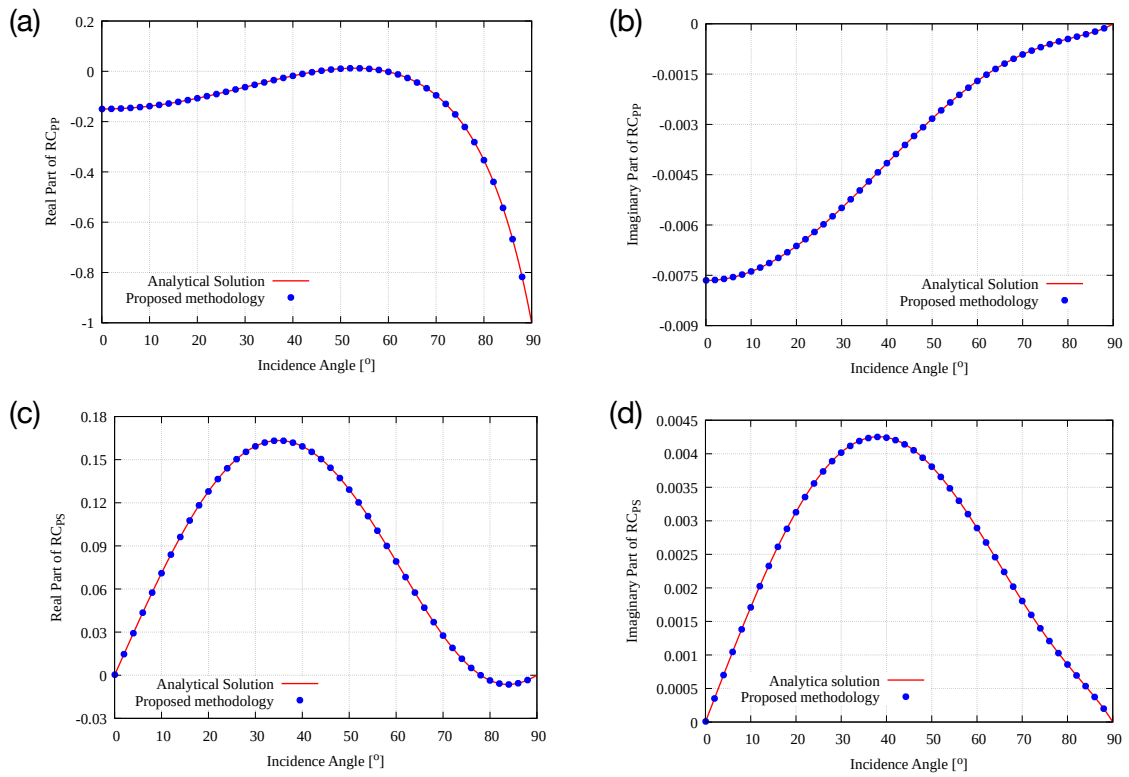

Figure A.1. Comparison between (a, b) P-wave and (c, d) S-wave reflection coefficients computed using the proposed methodology and those obtained with an analytical solution (Carcione 1997) for an HTI viscoelastic medium overlain by an isotropic elastic medium.

grains a bulk modulus $K_s^b = 37$ GPa and a density $\rho_s^b = 2650$ Kg/m^3. For the dry frame, we use a porosity $\phi^b = 0.15$, a permeability $\kappa^b = 1$ mD, a drained-frame bulk modulus $K_m^b = 13.5$ GPa, and a drained-frame shear modulus $\mu_m^b = 20$ GPa. For the fractures, we consider a specific fracture surface per unit volume of 1 m^{-1} and we assume that, at the grain level, the physical properties are the same as those of the background. For the dry-frame properties of the fractures, we consider normal and tangential weaknesses equal to 0.2 and we set the porosity to $\phi^f = 0.8$ and the permeability to $\kappa^f = 100$ D. Both the background and the fractures are saturated with water with a bulk modulus K_w=2.25 GPa, a density ρ_w=1090 Kg/m^3, and a shear viscosity $\eta_w = 0.001$ Pa $\cdot$ s. The fractures are assumed to be oriented in a way such that the effective medium has horizontal transverse isotropy (HTI).

The properties of the overlaying isotropic elastic medium are computed based on Gassmann's equations (Mavko et al. 1998). We consider for the solid grains a bulk modulus $K_s^b = 37$ GPa and a density $\rho_s^b = 2650$ Kg/m^3. For the dry frame, we use a porosity $\phi^b = 0.05$, a drained-frame bulk modulus $K_m^b = 28.12$ GPa, and a drained-frame shear modulus $\mu_m^b = 30.4$ GPa. The saturating pore fluid has properties identical to those employed for the fractured medium.

The resulting stiffness coefficients of the two media are then used in the reflectivity problem for comparison with an analytical solution. We consider a single frequency of 130 Hz, which coincides with the frequency of the maximal attenuation of the viscoelastic formation. Figure A.1 shows a comparison of the reflection coefficients obtained using the proposed methodology with those given by equation 54 of Carcione (1997). We observe excellent agreement between the two approaches, thus indicating that the proposed methodology has been correctly derived and implemented.

APPENDIX B: CONVERGENCE OF MONTE CARLO APPROACHES

Figures B.1 and B.2 show the standard deviations of the reflection coefficients as a cumulative function of the number of realizations for all the scenarios considered in this paper and for incidence angles of 0^o, 25^o, 50^o and 75^o. We observe that, in all cases, the standard deviations show very small fluctuations after 30 realizations, thus indicating that the convergences of the considered Monte Carlo analyses approach (Rubino et al. 2009).

ACKNOWLEDGMENTS

J.G.R. acknowledges the financial support received from the Agencia Nacional de Promoción Científica y Tecnológica of Argentina (PICT 2017-2976). This project has received funding from the Swiss National Science Foundation (grants 200020-178946 and 196037) and from the European Union Horizon MSCA-RISE 2020 project DISCO2 STORE, grant agreement No. 101007851. The authors gratefully acknowledge comments and suggestions from Enru Liu and an anonymous referee, which helped to improve this work.

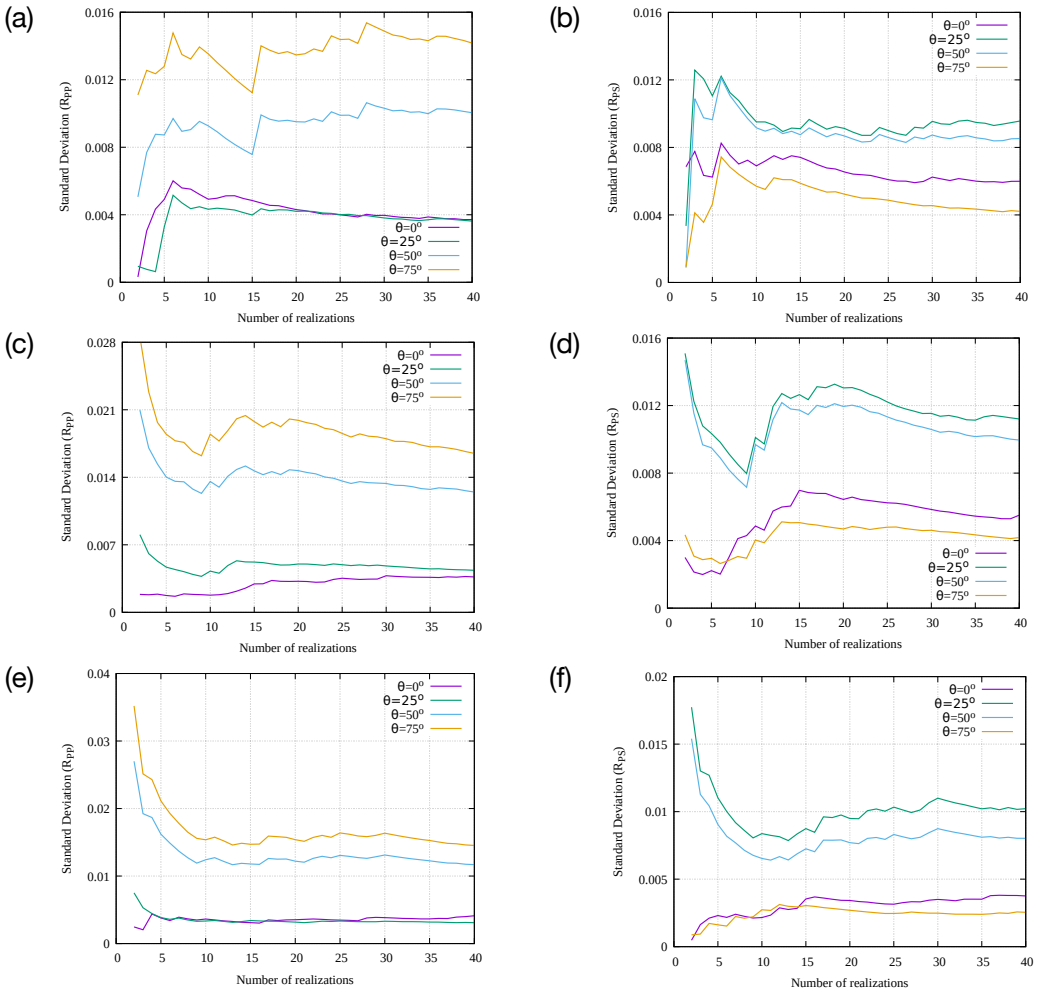

Figure B.1. Standard deviations of the reflection coefficients as functions of the number of realizations in the low-connectivity scenario for fracture intersection angles of (a, b) 45^o, (c, d) 60^o, and (e, f) 75^o. Panels (a), (c), and (e) correspond to the P-wave reflection coefficient, while panels (b), (d), and (f) show the responses for the S-wave reflection coefficient. Colors denote different incidence angles.

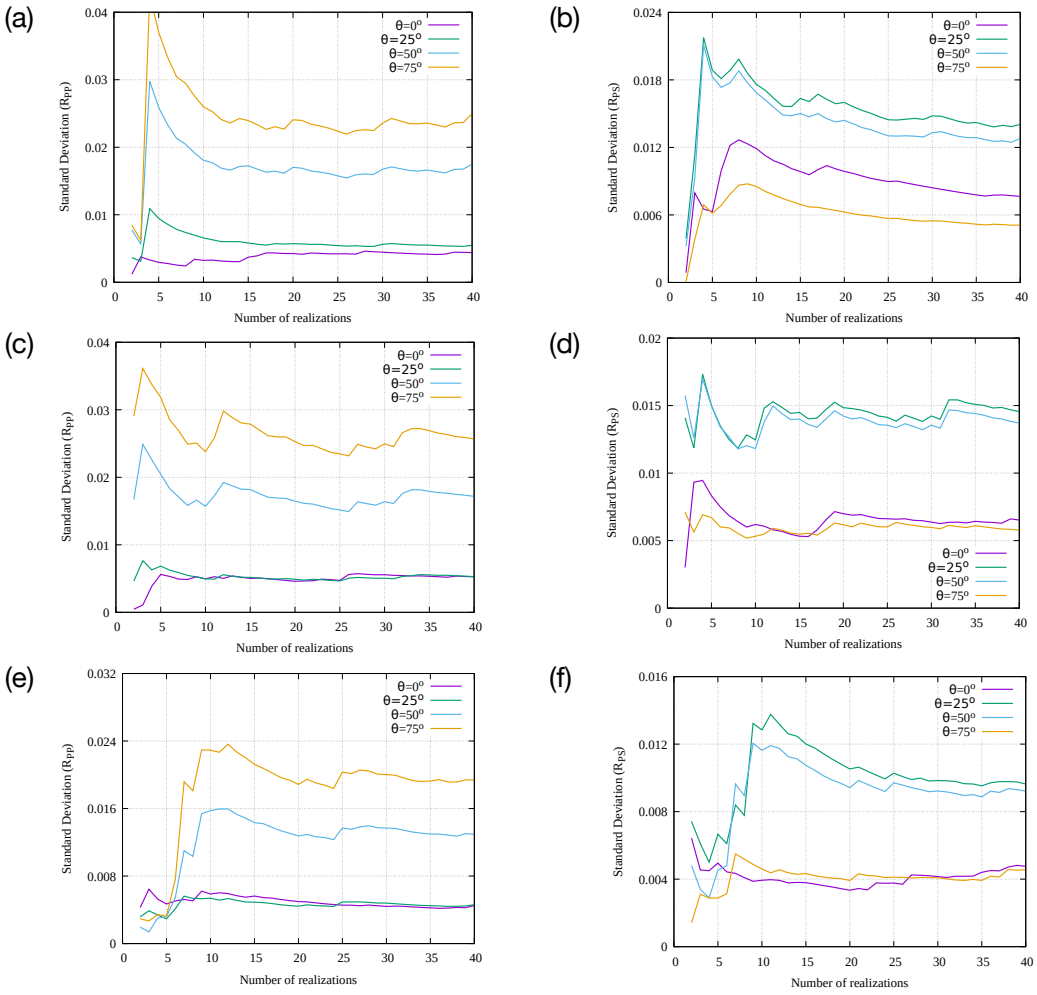

Figure B.2. Standard deviations of the reflection coefficients as functions of the number of realizations in the high-connectivity scenario for fracture intersection angles of (a, b) 45^o, (c, d) 60^o, and (e, f) 75^o. Panels (a), (c), and (e) correspond to the P-wave reflection coefficient, while panels (b), (d), and (f) show the responses for the S-wave reflection coefficient. Colors denote different incidence angles.